Mechanical spectroscopy study of as-cast and additive manufactured AlSi10Mg

Mechanical spectroscopy study of as-cast and additive manufactured AlSi10Mg

M.Cabibbo[1], R. Montanari[2,*], A. Pola[3], M. Tocci[3], A. Varone[2]

[1]: Dipartimento di Ingegneria Industriale e Scienze Matematiche (DIISM), Università Politecnica delle Marche, Via Brecce Bianche 12, 60131 - Ancona, Italy;

[2]: Dipartimento di Ingegneria Industriale, Università di Roma "Tor Vergata", Via del Politecnico 1, 00133- Roma, Italy

[3]: Dipartimento di Ingegneria Meccanica e Industriale, Università di Brescia, Via Branze 38, 25123, Brescia, Italy

* Corresponding author (Roberto Montanari; e-mail: roberto.montanari@uniroma2.it)

Abstract. The AlSi10Mg alloy produced by casting (AC) and additive manufacturing (AM) technology of laser powder bed fusion (L-PBF) has been investigated through mechanical spectroscopy (MS). In addition to the grain boundary peak P_{GB} the Q^{-1} curves of both materials exhibit two other relaxation peaks, *P1* (H = 0.8 ± 0.05 eV; $\tau_0 = 10^{-11 \pm 1}$ s) and *P2* (H = 1.0 ± 0.05 eV; $\tau_0 = 10^{-13 \pm 1}$ s), depending on the interaction of dislocations with solute elements (Si and Mg). Relaxation strengths of *P1*, *P2* and P_{GB} of AM alloy are greater than those of the AC one owing to the finer structure of Al cells and the higher amount of Si and Mg in supersaturated solid solution induced by the rapid solidification typical of the L-PBF process. After successive MS test runs relaxation strengths of *P1* and *P2* peaks in both the examined materials decrease due to the precipitation of Si atoms and dislocation density recovery. Such decrease is more pronounced in AM alloy where change of cell shape and increase of cell size is observed. Dynamic modulus of AM alloy exhibits an anomalous trend in the first test run that is no more present in successive runs. The irreversible process giving rise to such anomalous behavior is the closure of pores of nanometric size.

Keywords: AlSi10Mg, Casting, Additive manufacturing, Microstructure, Mechanical spectroscopy, XRD, Electron microscopy

1. Introduction

The microstructure of AlSi10Mg alloy produced by laser powder bed fusion (L-PBF) technology has been widely investigated in recent years [1-2]. The rapid solidification (up to 10^7 K/s [3]) typical of this process leads to the formation of an extra-fine structure, consisting of Al-matrix cells surrounded by a network of Si particles. The Al-matrix is a supersaturated solid solution containing Si atoms

above the equilibrium concentration [4]. Furthermore, networks of entangled dislocations were also observed in the Al matrix, which formed as a result of the fast solidification [5]. Moreover, Mg_2Si precipitates and Si dispersoids can be observed whenever the re-heating of the material during subsequent melting of successive layers is sufficient to enhance diffusion and precipitation phenomena [4-6]. This is often referred to as intrinsic heat treatment due to the repeated thermal cycles.

The layer-by-layer growing of the bulk parts is responsible for a hierarchical structure [7-9], as widely observed in various alloy manufactured by L-PBF technologies [10-11]. In fact, besides the abovementioned micro or submicrometric features, a fine grain structure can be identified [8]. Moving to a higher level, melt pools (or scan tracks) associated to the progressive melting and solidification of small volume of material under the effect of the laser (or other energy source) are observed [12].

All these features contribute to the high strength of this material in as-built condition owing to different strengthening contributions from solid solution, dislocations, grain boundaries and Orowan mechanism due to the presence of fine precipitates [4,13].

The main drawbacks related to the rapid solidification are the high residual stresses [14], that can cause distortion or cracking of the component, and the anisotropic mechanical response related to the layer over layer structure [15]. Therefore, heat treatment is often necessary to mitigate these detrimental manufacturing effects [16-17]. T6 heat treatment is reported to remove residual stresses and significantly reduce material anisotropy [18], although it generally reduces mechanical strength due to the coarsening of microstructure [18-19]. In addition, gas porosities present in the as-built material can grow during solution treatment leading to a remarkable decrease in the part density [16,20].

Recently, direct aging or low temperature annealing (in the range 373-523 K) have been proposed to recover residual stresses and reduce dislocation density without a significant alteration of the fine cellular structure of the alloy and porosity level [21-22]. This is crucial since the disruption of the Si network and the coarsening of the microstructure after heat treatment above 573 K is responsible for a marked decrease in strength. For this reason, a deep investigation of microstructural evolution during exposure to this temperature range (373-523 K) is crucial to identify and then to set the proper heat treatment parameters. Beside this, applications that involve exposure of the components to this temperature range cannot be excluded, given that AlSi10Mg alloy is often used in the automotive and aerospace industry. Therefore, the microstructural characterization as a function of temperature can also offer a precious support to enhance the use of this alloy for high-temperature applications.

The effect of different heat-treatment conditions on the impact behavior of an additive manufactured AlSi10Mg alloy has been studied by some of the present authors [23]. High-temperature mechanical behavior of AlSi10Mg alloy was investigated by Uzan et al. [24] up to 673 K. The material was tested after stress relief treatment and the mechanical response changed above 473 K since the plastic behavior became dominant. However, the stress relief treatment is known to affect the as-built microstructure and therefore also the mechanical response is expected to be different under as-built condition. Similarly, Cao et al. [13] performed in-situ SEM and EBDS analysis to investigate the microstructural evolution up to 673 K of selective laser melted AlSi10Mg. Little changes in the main microstructural features were identified up to 473 K. On the contrary, when the temperature reached 573 K and above, the coarsening and precipitation of Si particles was instead identified in Al matrix. The Si particle formation was responsible for a decrease of solid solution strengthening during high-temperature tensile testing.

Another study [25] focused on the characterization of samples exposed to temperatures in the range of 393-453 K and then cooled down to be tested at room temperature. It was found that Si particles precipitate in the Al matrix during holding at 433 K. This is caused by the high content of Si retained in the supersaturated solid solution after production. On the other hand, the network of coarser Si particles remains unaffected at this temperature. This consists basically in an aging treatment, which results in an increase in strength and a limited ductility when the alloy is subsequently tested at room temperature. In general, good thermal stability of the alloy when exposed to 433 K for several hours was assessed. In addition, in-situ analysis showed the breaking up of the Si network and formation of Si precipitates already above 433 K, together with the evolution of Si clusters and nanoparticles, mainly changing their coherency with the matrix [26]. This appears in contrast with previous studies where no significant changes in the microstructure were detected below 473 K [13,21,24].

In this work mechanical spectroscopy (MS) has been used to get additional information regarding the anelastic behavior of the alloy. MS is a dynamic technique for the characterization of material properties and provides information that can not be obtained otherwise. The formal theory of anelasticity can be found in the book of Nowick and Berry [27] while an exhaustive collection of data taken from literature is reported in that of Blanter et al. [28]. Dynamic modulus and internal friction have been measured up to 790 K and the results correlated to microstructural changes investigated by light microscopy (LM), X-ray diffraction (XRD), transmission (TEM) and scanning (SEM) electron microscopy. The same experiments and analyses were carried out also on samples with the same chemical composition but produced by gravity casting. As shown in a preliminary study [29], the comparison is useful to better understand the correlation between manufacturing process, microstructure and properties.

2. Experimental

The AlSi10Mg alloy has been investigated in two different conditions: as-cast (AC) and prepared by additive manufacturing in as-built condition (AM). The nominal alloy composition is reported in Table 1.

Table 1. Nominal composition (wt. %) of the investigated alloy.

Composition (wt%)	Si	Mg	Fe	Mn	Al
AlSi10Mg	9-11	< 0.55	< 0.55	< 0.45	balance

The AM material was manufactured in form of plates (x = 30 mm, y = 2 mm, z = 70 mm) by using an EOS M290 machine and EOS AlSi10Mg powders with particles size is in the range 25 - 70 μm were used. The build direction was the z direction. The powder bed with layer thickness of 30 μm was selectively melted under Argon atmosphere using laser power of 370 W and scanning speed of 1300 mm/s. The platform was preheated at 80 °C.

The AC samples were obtained from by gravity casting in a steel permanent mold.

The density of AM material, determined by weight and volume measurements, is 2.39 ± 0.03 g/cm^3 namely about 90% of that of the AC bulk alloy (2.65 ± 0.03 g/cm^3).

Both types of samples (AC and AM) have been tested without preliminary heat treatments.

MS tests were made in the temperature range 300-790 K with a constant heating rate of 1.5 K/min by using an automated vibrating reed analyzer (VRA 1604, CANTIL s.r.l.) [30] and operating in resonance conditions with frequency f in the range 150-2000 Hz. The samples in form of reeds (60.7 mm length, 6.9 mm width, 2 mm thickness) were mounted in free-clamped mode and put in resonance by an electrostatic excitation with strain amplitude of 5 x 10^{-5}. Experiments were performed in a vacuum chamber under a 10^{-6} mbar pressure.

The damping parameter Q^{-1} was determined from the logarithmic decay of the flexural vibrations after turning off the exciting signal:

$$Q^{-1} = \frac{1}{k\pi} \ln\left(\frac{A_n}{A_{n+k}}\right) \quad (1)$$

where A_n and A_{n+k} *are* the amplitudes of the n-th and $n+k$-th oscillation. Dynamic modulus E and resonance frequency f are related by the equation:

$$E = \frac{48\,\pi^2 \rho L^4}{m^4 h^2} f^2 \quad (2)$$

L and *h* are the length and thickness of the sample, respectively, $m = 1.875$ is a constant and ρ is the material density.

XRD measurements were carried out on both materials in the original condition and after MS test runs by using the Cu-Kα radiation ($\lambda = 0.15408$ nm). Diffraction patterns were collected in the 2Θ angular range 18°- 118° with 2Θ steps of 0.05° and counting time of 10 s per step.

The amount of Si phase was determined by the integrated peak intensity of the Al and Si phases in diffraction pattern according to the direct comparison method [31].

To determine the dislocation density in Al phase, high precision peak profiles of the most intense reflections were recorded with 2Θ steps of 0.005° and counting time of 20 s per step and analyzed through the Warren-Averbach procedure [32]. Once determined the main contributions to peak broadening, namely micro-strains ε related to dislocation structures and size of coherently diffracting domains, the dislocation density ζ was calculated through the Williamson-Smallman relationship [33]:

$$\zeta = \frac{\Xi \varepsilon^2}{F b^2} \tag{3}$$

being $\Xi = 16.1$ a constant, $F \approx 1$ a factor depending on the interaction of dislocations and $b = 0.2856$ nm the modulus of Burgers vector.

Moreover, from the precision XRD peak positions the lattice parameter *a* was determined by using the $\cos^2\theta$ method [31].

The original structure of the samples was investigated by light microscopy (LM) and scanning electron microscopy (SEM) with energy dispersive spectroscopy (EDS). A Zeiss™ Supra-40® field-emission gun scanning electron microscope (FEG-SEM) was used for the porosity inspections in AM alloy, in both as-build condition and after MS tests. FEG-SEM surface samples were prepared by etching with a Keller reagent at room temperature for 20-30 s.

Transmission electron microscopy (TEM) was used to describe the characteristics and the evolution of lattice defects before and after MS test runs. TEM specimens were mechanically polished down to 0.25 μm by means of diamond paste, dimpled, and then prepared using a precise ion polishing device (PIPS, GATAN™) working at 12 V and by setting the Ar^+ beam at decreasing incident angles from 8 to 4° respect to the thin foil surface. All TEM inspections were carried out by using a Philips™ CM-200® microscope equipped with a double-tilt specimen holder with liquid nitrogen cooling stage.

3. Results

3.1. As-cast alloy

AlSi10Mg manufactured by foundry processes has been largely used in several industrial applications, thus the AC alloy is considered here the reference material. As shown by the LM micrograph in Figure 1 (a), AC alloy exhibits a rough Al dendritic structure surrounded by a fine modified eutectic. Particles with elongated shape and size below 10 μm are also observed. The chemical composition of these particles, whose morphology is displayed at higher magnification by the SEM image in (b), has been examined by EDS. They resulted to contain variable amounts of Al (65-80 wt.%), Si (7-12 wt.%), Fe (7-17 wt.%) and Mn (5-10 wt.%). For example, the EDS analysis carried out on some particles indicated in Figure 1 (b) are reported in (c). It is noteworthy that they are rich of Fe and Mn while Mg is not present. Inside the Al matrix dislocations tend to arrange forming cells with mean size of about 1 μm, as indicated by TEM observation (Figure 1 d).

Figure 2 shows the Q^{-1} and dynamic modulus E curves obtained by testing the same AC sample in three successive MS test runs. Each test run consisted of a heating-cooling cycle from room temperature to 790 K. Dynamic modulus curves are normalized to the initial value at room temperature E_0.

Q^{-1} curves exhibit a peak at 753 K that is the grain boundary peak P_{GB}, firstly observed by Kê in bulk Al [34] and then in many other Al alloys (e.g. see the review in [28]). By subtracting to experimental data the exponential background and P_{GB} peak, the presence of two other peaks of lower intensity at 540 and 640 K is evident, hereinafter termed *P1* and *P2*, respectively.

Q^{-1} curves vs. temperature measured in each test run are substantially the same during heating and cooling and dynamic modulus curves show a slope change in correspondence of the peaks. Moreover, as shown by the example reported in Figure 3, the central position of the peaks changes in tests carried out at different resonance frequencies thus *P1* and *P2* are relaxation peaks.

As shown by Figure 4, the values of Q^{-1} are a little lower in the test runs successive to the first one, but the shape of the curve does not change.

To fit the experimental Q^{-1} data the peaks *P1*, *P2* and P_{GB} have been treated as Debye peaks while the background has been considered as an exponential function of temperature. On these grounds the fitting curve results to be the sum of four contributions:

$$Q^{-1} = \frac{\Delta_1}{2}\sec h\left[\left(\frac{H_1}{k}\right)\left(\frac{1}{T}-\frac{1}{T_1}\right)\right] + \frac{\Delta_2}{2}\sec h\left[\left(\frac{H_2}{k}\right)\left(\frac{1}{T}-\frac{1}{T_2}\right)\right] + \\ + \frac{\Delta_{GB}}{2}\sec h\left[\left(\frac{H_{GB}}{k}\right)\left(\frac{1}{T}-\frac{1}{T_{GB}}\right)\right] + ae^{-b/kT} \quad (4)$$

where $Q^{-1}_{back} = a\ exp(-b/kT)$ is the background, k is the Boltzmann constant, Δ the relaxation strength ($\Delta/2$ is the maximum peak intensity), H_1, H_2 *and* H_{GB} the activation energies of the peaks *P1, P2* and P_{GB}, T_1, T_2 and T_{GB} their central positions. Since a relaxation peak takes place if the following condition is satisfied:

$$\omega\tau = \omega\tau_0 e^{H/kT} = 1 \quad (5)$$

being $\omega = 2\pi f$, τ the relaxation time and τ_0 its pre-exponential factor, the activation energies H_1, H_2 and H_{GB} have been determined by means of Eq. (5) from the shift of peak temperature in MS tests with different resonance frequencies. The values of activation energy H and pre-exponential factor τ_0 of the peaks are reported in Table 2.

Table 2. Activation energy H and pre-exponential factor τ_0 of the peaks *P1*, *P2* and P_{GB}.

Q^{-1} peaks	Activation energy H (eV)	τ_0 (s)
P1	0.8 ± 0.05	$10^{-11 \pm 1}$
P2	1.0 ± 0.05	$10^{-13 \pm 1}$
P_{GB}	1.3 ± 0.05	$10^{-13 \pm 1}$

The relaxation strengths of *P1, P2* and P_{GB}, and the parameters *a* and *b* of background curve have been adjusted to get the best fitting of the experimental curves. Figure 4 displays the fitting of Q^{-1} curves measured in three successive test runs made on the same sample. Table 3 reports the maximum intensity ($Q^{-1}_{MAX} = \Delta/2$) of the peaks *P1*, *P2* and P_{GB}, and the values of the parameters *a* and *b* of the exponential background which have been used to get the best fit of experimental data. Even if Q^{-1}_{MAX} variations in successive test runs are small, not much larger than the experimental error, the intensity of peaks *P1, P2* and P_{GB} tends to decrease while the background substantially does not change.

Table 3. As-cast (AC) alloy: peak intensity (Q^{-1}_{MAX}) of the peaks *P1*, *P2* and $P_{GB,}$ and the parameters *a* and *b* of the exponential background used to fit of the experimental Q^{-1} curves. Errors of Q^{-1}_{MAX} have been estimated to be ± 0.001 for *P1* and *P2*, and ± 0.002 for P_{GB}, respectively.

AC alloy	$Q^{-1}_{MAX} = \Delta/2$			Background	
Peak	*P1*	*P2*	P_{GB}	*a*	*b*
1st run	7.54×10^{-3}	9.24×10^{-3}	3.89×10^{-2}	4.0×10^{4}	9.9×10^{-1}
2nd run	5.10×10^{-3}	7.10×10^{-3}	3.40×10^{-2}	3.8×10^{4}	9.9×10^{-1}
3rd run	4.80×10^{-3}	7.10×10^{-3}	3.32×10^{-2}	3.3×10^{4}	9.9×10^{-1}

3.2. Additive manufactured alloy

The microstructure of AM alloy is quite different, and Figure 5 (a-b-c) shows at different magnification its typical features. In the horizontal section (a) it is possible to observe the pattern of laser scan tracks while the vertical section (b) displays the semi-circular shape of melt pools (average width ~130 μm and depth ~70 μm). As shown in a previous work on the same material [23], the Al grains (5-10 μm wide and several tens of μm long) inside the melt pool are elongated in the building direction whereas near its boundary finer equiaxed grains of ~10 μm are observed. At higher magnification each grain exhibits a finer sub-structure of cells decorated by eutectic Si (c). The average size of the cells is ~ 400 nm, *i.e.*, about one order of magnitude lower than that of grains. TEM micrograph in Figure 6 (a-b) shows Si particles of very small size (100-150 nm) and irregular shape. Moreover, the material exhibits a certain degree of porosity (~10%) that consists of two types of pores: pores of ~ 10 μm with irregular shape (Figure 7 a) and a lot of spherical pores of nanometric size (Figure 7 b).

The Q^{-1} curves of the AM alloy measured in three successive test runs are similar to those of the AC one and have been fitted in the same way. The results are shown in Figure 8 and data used for the best fittings are reported in Table 4. The intensities of the peaks *P1*, *P2* and P_{GB} are always higher in the AM alloys than in the AC one and also in this case a slight decrease is observed in successive test runs, in particular after the 3rd run.

Table 4. Additive manufactured (AM) alloy: peak intensity (Q^{-1}_{MAX}) of the peaks *P1*, *P2* and $P_{GB,}$ and the parameters *a* and *b* of the exponential background used to fit of the experimental Q^{-1} curves. Errors of Q^{-1}_{MAX} have been estimated to be ± 0.001 for *P1* and *P2*, and ± 0.002 for P_{GB}, respectively.

AM alloy	$Q^{-1}_{MAX} = A/2$			Background	
Peak	*P1*	*P2*	P_{GB}	*a*	*b*
1st run	1.05×10^{-2}	1.52×10^{-2}	9.47×10^{-2}	9.95×10^{4}	1.04
2nd run	1.10×10^{-2}	1.53×10^{-2}	8.45×10^{-2}	9.95×10^{4}	1.04
3rd run	8.54×10^{-3}	1.22×10^{-2}	7.94×10^{-2}	9.95×10^{4}	1.04

The different original structure of the two materials and successive evolution is also evidenced by XRD.

Figure 9 a) compares the XRD patterns of AC and AM alloys: it is evident that the Si reflections are more intense in AC than in AM alloy. In the angular range 37-46° the pattern of AC alloy shows a couple of peaks of very low intensity, at the limit of detectability. Figure 9 b) displays this part of the XRD pattern recorded with higher angular resolution (2θ steps of 0.005° instead of 0.05°) and longer counting time per step (20 s instead of 2 s) to evidence these peaks which, according to the JCPDS-ICDD X-ray database [35], have been identified as the {300} and {301} / {212} reflections of the $Al_9Fe_{0.84}Mn_{2.16}Si$ compound (File 42-1206) with hexagonal structure (a = 0.75198 nm and c = 0.77688 nm). In fact, the detected peak positions are very close to those of other compounds of Al and Fe ($Al_{13}Fe_4$ and $Al_{76.7}Fe_{24}$) or Al and Mn (Al_6Mn) but the EDS microanalysis indicates that the particles contain always all the elements (Al, Si, Fe and Mn) in variable amounts. Therefore, from XRD it is reasonable to conclude that the particles with elongated shape shown in Figure 1 (b) are quite similar to $Al_9Fe_{0.84}Mn_{2.16}Si$ with some deviations depending on the variable composition.

Table 5 reports the Si volume fraction, the lattice parameter of Al phase and its dislocation density ζ determined through XRD in different samples.

Table 5. Si volume fraction, lattice parameter of Al phase and dislocation density ζ of as-prepared as-cast (AC) and additive manufactured (AM) alloys and after MS test runs.

	AC alloy				AM alloy			
Treatment	As-prepared	1st test run	2nd test run	3rd test run	As-built	1st test run	2nd test run	3rd test run
Si volume (%)	10.1 ± 0.3	11.6 ± 0.3	11.7 ± 0.3	11.7 ± 0.3	9.1 ± 0.3	9.7 ± 0.3	9.9 ± 0.3	10.2 ± 0.3
Lattice parameter (nm)	0.4050 ± 0.0001	0.4051 ± 0.0001	0.4051 ± 0.0001	0.4051 ± 0.0001	0.4045 ± 0.0001	0.4048 ± 0.0001	0.4049 ± 0.0001	0.4050 ± 0.0001
Dislocation density ζ (cm^{-2})	(6.0 ± 1) x 10^{10}	(1.7 ± 1) x 10^{9}	(1.6 ± 1) x 10^{9}	(1.6 ± 1) x 10^{9}	(5.6 ± 1) x 10^{10}	(3.3 ± 1) x 10^{10}	(1.3 ± 1) x 10^{10}	(1.1 ± 1) x 10^{10}

3.3. Modulus anomaly of additive manufactured alloy

A relevant phenomenon has been observed in the 1st test run of AM alloy, it consists in the anomalous trend of dynamic modulus. As temperature increases, the modulus is expected to monotonically decrease owing to anharmonicity effect, however in this case at ~ 445 K it starts to increase, exhibits a maximum at ~ 485 K, then decreases again. This behavior, which is typical of all the examined AM samples independently on the specific resonance frequency, is no more observed in the successive test runs. Figure 10 shows the curves of dynamic modulus normalized to the value measured at room temperature in the 1st test run. After the 1st run the modulus results to be increased of about 7% and is not further modified by the successive test runs.

To clarify the origin of such phenomenon, the density of the material has been measured after the 1st test run and it resulted increased from 2.39 g/cm^3 (as-built material) to 2.52 g/cm^3. In the successive test runs the density substantially does not change.

Other structural changes are highlighted by XRD and TEM inspections. XRD patterns of as-built AM alloy, before and after the 1st test run, are reported in Figure 10. The XRD pattern comparison displays an intensity increase of Si peaks after the 1st run corresponding to a variation of Si volume fraction from 9.1 to 9.7 % (Table 5). This indicates that the sample heating during the test favors the precipitation of Si that is in oversaturation in the Al phase of as-built alloy. Moreover, TEM micrographs in Figure 12 show that the elongated cells of the original structure have been replaced by near equiaxed cells (a) of larger size (~ 1 μm); in concomitance the pores of smaller size disappear and only those of larger size survive (b). Figure 12 (c) shows an array of kinked dislocations that is a typical feature observed also in both types of samples before and after MS test runs.

4. Discussion

4.1. The relaxation peaks

The Q^{-1} curves of both alloys, AC and AM, exhibit three relaxation peaks (*P1, P2* and P_{GB}) and an exponential background.

The relaxation strength of grain boundary peak P_{GB} is higher in the AM alloy than in the AC one because AM alloy exhibits a finer and more complex structure of grains and cells (Figures 1 and 2). Q^{-1} depends on the total grain boundary area:

$$Q^{-1} = \frac{1}{2\pi}\frac{\Delta W}{W} \tag{6}$$

being W the maximum stored energy and ΔW the energy loss in a single vibration cycle per unit volume. Q^{-1} is directly proportional to the term A_{GB} / V, i.e. the total area of grain boundaries A_{GB} per

unit volume, where the term “grain boundary” includes low and high angle grain boundaries, and cell boundaries.

Tables 3 and 4 show that the relaxation strength of peak P_{GB} of both alloys diminishes after MS test runs and the major decrease is observed in AM alloy. The result is in agreement with TEM observations (Figures 6 (a) and 12 (a)) showing a change of cell shape and an increase of cell size after the 1st test run. As expected, the AM alloy undergoes greater changes owing to the specific conditions of the preparation process leading to an unstable microstructure.

Apart from the grain boundary peak P_{GB} the other peaks (*P1* and *P2*) are not observed in pure Al thus they seem connected to physical mechanisms involving alloying elements, either in solid solution or in form of compounds. Moreover, activation energy and relaxation time of *P1* ($H = 0.8 \pm 0.05$ eV; $\tau_0 = 10^{-11 \pm 1}$ s) and *P2* ($H = 1.0 \pm 0.05$ eV; $\tau_0 = 10^{-13 \pm 1}$ s) are typical of dislocation mechanisms. These considerations suggest that the peaks *P1* and *P2* are due to relaxation processes involving interaction of alloying elements with dislocation structures.

Specific MS data of the AlSi10Mg alloy are not reported in literature, however the binary systems Al-Si and Al-Mg have been extensively investigated [28].

Pichler et al. [36-3] studied the system Al-Si and found a relaxation peak with activation energy $H = 1.14$ eV and relaxation time $\tau_0 = 2.4 \times 10^{-14}$ s, i.e. values very close to those of peak *P2* observed in present experiments. They explained the peak as an effect of the increased transversal diffusivity of solute atoms in proximity of dislocation core and developed a model reported in [36]. A relaxation peak with similar characteristics ($H = 1.1$ eV, $\tau_0 = 4.0 \times 10^{-14}$ s) was reported by Atodiresei et al. [38] for the Al-4 at% Mg alloy and was discussed in terms of a solute-dislocation interaction model. Benyahia et al. [39] attributed to a Zener relaxation mechanism a peak with $H = 1.09$ eV, $\tau_0 = 2.0 \times 10^{-14}$ s observed in the Al-12 wt% Mg alloy. Golovin et al. [40-44] investigated anelastic processes occurring in Al-Mg alloys in an extended range of Mg concentrations (up to 12 wt%) and under different heat treatment conditions. They detected a peak, whose intensity is higher after quenching than after annealing, with characteristic values of H and τ_0 a little changing with treatment conditions but always close to those of the *P2* peak measured by us and concluded that it is stipulated by a thermally activated process.

To understand the origin of *P2* peak the information about atoms in solid solution and dislocation density provided by XRD has been considered. It is noteworthy to remind that alloying elements in solid solution change the lattice parameter of the Al phase, specifically it is increased by Mg and decreased by Si, Mn and Fe [45]. The variations are substantially proportional to the relative difference of atomic radii of solute and Al atoms. The lattice parameter of the AlSi10Mg alloy in conditions of thermodynamic equilibrium (0.40515 nm) [46] is larger than that of pure Al (0.40494

nm) and such difference depends on Mg atoms in large part in solution in the Al phase. In fact, apart from the Al solid solution the other phases are the eutectic Si and the particles with elongated shape which contain Al, Si, Mn and Fe but not Mg (see Figure 1).

From present investigation (Table 5) the values of as-prepared AC and AM alloys are 0.4050 nm and 0.4045 nm, respectively, namely lower than that of the alloy in equilibrium. The result indicates that a certain amount of Si remains in solution in the Al phase in both alloys and is higher in the AM one owing to the fast cooling of liquid metal typical of this manufacturing process. This is confirmed by the intensity of Si reflections in XRD patterns, which are stronger in AC alloy than in AM one (Figure 8). An excess of Si in AM alloy was previously reported by other investigators [46]. During MS tests the sample heating induces the precipitation of Si in both alloys and after the 1st run the value of equilibrium is substantially reached in the AC alloy but not in the AM one.

Data in Table 5 indicate that the dislocation density ζ of both as-prepared alloys diminishes after MS test runs. Therefore, the change of *P2* relaxation strength after MS test runs depends on both the decrease of dislocation density and concentration of atoms in solid solution. XRD results suggest that the decrease of atoms in solid solution is substantially due to the precipitation of Si atoms.

For dislocation models like that of Pichler et al. [37] the relaxation strength Δ is given by:

$$\Delta \approx \frac{\zeta . l^2}{10} \tag{7}$$

being ζ the dislocation density and l the mean distance between dislocation pinning points. By combining the values of relaxation strength values (Tables 3 and 4) and dislocation density (Table 5) the mean link length l of dislocation segments for both the materials in different conditions results to be of the order of some tens of nanometers, namely in good agreement with the mean distance of precipitates observed by TEM. The formation of new precipitates of Si following MS test runs contributes to reduce the relaxation strength because the mean distance between dislocation pinning points l decreases.

An alternative explanation of peak *P2* could be due to a Zener mechanism. On the basis of relaxation parameters this can not be excluded, however it is noteworthy that Zener peaks have been observed in Al-Mg alloys with a quite larger Mg content than that of our alloy [28]. For example, Benyahia et al. [39] investigated the Al-12 wt% Mg alloy and the peak was observed only after solution treatment and quench when a lot of Mg atoms are in supersaturated solid solution. On these grounds we do not believe that the origin of peak *P2* can be ascribed to a Zener mechanism.

To explain peak *P1* reference is done to a study on the system Al-Mg due to Kê and Tan [47] who reported a peak with $H = 0.7 \pm 0.1$ eV and $\tau_0 \approx 10^{-8}$ s in Al alloys with different Mg contents (0.02, 0.12, 0.55, 1.1, 6 wt%). Its origin was associated to the stress induced re-orientation of Mg atom pairs

in dumbbell configuration enhanced by the stress field of mobile kinks in dislocations present in the Al matrix. Such explanation is based on the activation energy of 0.8 eV, unusually low for a pure Zener relaxation, and considers the role played by the stress field of mobile dislocation kinks as those displayed in the TEM micrograph of Figure 12 c).

The slight decrease of *P1* relaxation strength observed in both materials after successive MS test runs is believed to be mainly due to the decrease of dislocation density.

In conclusion both peaks *P1* and *P2* are due to the interaction of dislocations with solute atoms (Mg or Si) and their relaxation strengths depend on both the dislocation density and the concentration of alloying elements in solid solution. Thermal cycling during MS tests favors the precipitation of alloying elements present in solid solution in concentration higher than that of thermodynamic equilibrium and the partial recovery of dislocation structures leading to a decrease of relaxation strengths of *P1* and *P2* peaks.

4.2. Dynamic modulus anomaly in AM alloy

An interesting phenomenon observed in our MS experiments is the anomaly of dynamic modulus exhibited by AM alloy in the 1st test run. The inversion in the decreasing trend occurs in the temperature range 445-485 K and results in a permanent variation of ~7% at the end of the complete heating-cooling cycle. The irreversible phenomenon is not observed in the successive test runs and is specific of the AM alloy since modulus of the AC alloy shows the typical monotonous decreasing trend vs. temperature (Figure 2).

To explain such phenomenon the microstructure inspections have been focused on the possible densification due to the closure of pores. In the as-built AM alloy TEM micrographs show arrays of pores of nanometric size aligned along the built direction (Figures 6 a) and 7 b); after the 1st test run they totally disappear (Figure 12 a and b) and the density results increased from 2.39 ± 0.03 g/cm^3 to 2.52 ± 0.03 g/cm^3, namely a value a little smaller than that of the AC bulk alloy (2.65 ± 0.03 g/cm^3). Figure 12 b) shows some pores of large size which are still present after the MS test run, thus it is not surprising that the density is a little lower than that of bulk alloy. However, each MS test run involves a cycle of heating up to 790 K and successive cooling to ambient temperature, hence TEM observations on samples after the 1st test run are not fully resolutive to associate the modulus anomaly occurring between 445 and 485 K to the closure of pores which could take place at higher temperature. Therefore, in some experiments the 1st run was interrupted when the samples reached the temperature of 485 K, they were immediately cooled down and then investigated by high-resolution FEG-SEM. The micrographs in Figure 13 (a-b-c) taken at high magnification show relevant differences of porosity before (a and b) and after (c) the heating up to 485 K. It resulted that the pores present in as-

built condition (Figure 13 a-b) disappear after heating (Figure 13 c). As a matter of fact, this result confirms that the modulus anomaly is connected to material densification; the given explanation is also supported by considerations regarding atom diffusion necessary for pore closure.

According to Eq. (2) the resonance frequency f is proportional to $(E/\rho)^{1/2}$ thus, assuming the relationship $E \propto \rho^2$ given by the Gibson-Ashby model [48], the variations of resonance frequency measured at room temperature before and after the 1st test run are always in good agreement with the observed change of density. Since the pore closure is a phenomenon driven by the diffusion of atoms in the Al matrix the random walk *RW* corresponding to the heating rate of 1.5 K/minute up to 500 K has been determined. For the temperature *T* and time *t*, *RW* can be written as:

$$RW = (6D\mathrm{t})^{1/2} \tag{8}$$

where *D* is the coefficient of auto-diffusion of Al given by:

$$D = D_0 \exp\left(\frac{-Q}{RT}\right) \tag{9}$$

being *R* the gas constant (1.987 cal $mol^{-1}K^{-1}$), D_0 = 3.5 x 10^{-4} mm^2 s^{-1} and *Q* = 28750 cal mol^{-1}.

In the case of present experiments temperature is not constant but increases with a rate of 1.5 K/minute thus the total *RW* is the sum of the *RW* of each step in the heating ramp. By integrating Eq. (8) with time steps *dt* of 20 s along the thermal path of the sample during heating from room temperature to 445 K, the temperature at which dynamic modulus starts to exhibit the anomalous behavior, the total *RW* results to be ~ 76 nm. Of course, the integration steps depend on the signal acquisition rate used in the experiments. The obtained *RW* value represents the radius of pores suppressed by the effect of sample heating and is close to that of smallest pores observed in the as-built AM alloy (Figure 7 b).

In the case the integration is extended at 485 K, corresponding to the upper limit of the temperature range where modulus anomaly occurs, the resulting *RW* is ~ 360 nm. Pores with radii greater than this value are still observed in the samples and are not suppressed by heating to higher temperature, most likely owing to oxidation of internal pore surfaces or presence of gas inside the pores.

5. Conclusions

The anelastic behavior of the AlSi10Mg alloy prepared by casting (AC) and additive manufacturing (AM) has been investigated and correlated to the specific microstructural features. The main results can be summarized as follows.

(i) In addition to the grain boundary peak P_{GB}, the Q^{-1} curves of AC and AM alloys exhibit two relaxation peaks, *P1* (H = 0.8 ± 0.05 eV; $\tau_0 = 10^{-11 \pm 1}$ s) and *P2* (H = 1.0 ± 0.05 eV; $\tau_0 = 10^{-13 \pm 1}$ s), due to the interaction of solute atoms with dislocations.

(ii) The origin of peak *P1* has been associated to the stress induced re-orientation of Mg atom pairs in dumbbell configuration enhanced by the stress field of mobile dislocation kinks while the peak *P2* is due to the effect of the increased transversal diffusivity of solute atoms in proximity of dislocation core.

(iii) Relaxation strengths of *P1, P2* and P_{GB} of AM alloy are greater than those of the AC one owing to the finer structure of Al cells and the higher amount of Si and Mg in supersaturated solid solution induced by the rapid solidification typical of the production process.

(iv) Relaxation strengths of P_{GB}, *P1* and *P2* in both the examined materials decrease after successive MS test runs, due to precipitation of Si atoms and dislocation density recovery. The decrease is more pronounced in AM alloy owing to its more unstable microstructure that after the 1st test runs evolves with change of cell shape and increase of cell size.

(v) Dynamic modulus of AM alloy exhibits an anomalous trend in the first test run that is no more present in successive runs. As shown by FEG-SEM observations and density measurements, the irreversible process giving rise to such an anomalous behavior is the closure of pores of nanometric size.

Acknowledgements

The authors are grateful to Mr. Piero Plini of Department of Industrial Engineering – University of Rome “Tor Vergata” for assistance in the preparation of samples used in MS tests.

References

[1] N.T. Aboulkhair, M. Simonelli, L. Parry, I. Ashcroft, C. Tuck, R. Hague, 3D printing of Aluminium alloys: Additive Manufacturing of Aluminium alloys using selective laser melting, Progress in Materials Science 106 (2019) 100578.

[2] J. Zhang, B. Song, Q. Wei, D. Bourell, Y. Shi, A review of selective laser melting of aluminum alloys: Processing, microstructure, property and developing trends, Journal of Materials Science & Technology 35(2) (2019) 270-284.

[3] P.A. Hooper, Melt pool temperature and cooling rates in laser powder bed fusion, Additive Manufacturing 22 (2018) 548-559.

[4] L. Zhou, A. Mehta, E. Schulz, B. McWilliams, K. Cho, Y. Sohn, Microstructure, precipitates and hardness of selectively laser melted AlSi10Mg alloy before and after heat treatment, Materials Characterization 143 (2018) 5-17.

[5] A. Hadadzadeh, B.S. Amirkhiz, M. Mohammadi, Contribution of Mg2Si precipitates to the strength of direct metal laser sintered AlSi10Mg, Materials Science and Engineering: A 739 (2019) 295-300.

[6] J. Wu, X.Q. Wang, W. Wang, M.M. Attallah, M.H. Loretto, Microstructure and strength of selectively laser melted AlSi10Mg, Acta Materialia 117 (2016) 311-320.

[7] Y.J. Liu, Z. Liu, Y. Jiang, G.W. Wang, Y. Yang, L.C. Zhang, Gradient in microstructure and mechanical property of selective laser melted AlSi10Mg, Journal of Alloys and Compounds 735 (2018) 1414-1421.

[8] X. Liu, C. Zhao, X. Zhou, Z. Shen, W. Liu, Microstructure of selective laser melted AlSi10Mg alloy, Materials & Design 168 (2019) 107677.

[9] A. Hadadzadeh, B. Shalchi Amirkhiz, A. Odeshi, J. Li, M. Mohammadi, Role of hierarchical microstructure of additively manufactured AlSi10Mg on dynamic loading behavior, Additive Manufacturing 28 (2019) 1-13.

[10] L. Tonelli, Revealing the Hierarchical Microstructure of Innovative Additively Manufactured Metal Parts with Conventional Light Microscopy, Metallography, Microstructure, and Analysis 10(2) (2021) 278-282.

[11] L.-E. Rännar, A. Koptyug, J. Olsén, K. Saeidi, Z. Shen, Hierarchical structures of stainless steel 316L manufactured by Electron Beam Melting, Additive Manufacturing 17 (2017) 106-112.

[12] Z.H. Xiong, S.L. Liu, S.F. Li, Y. Shi, Y.F. Yang, R.D.K. Misra, Role of melt pool boundary condition in determining the mechanical properties of selective laser melting AlSi10Mg alloy, Materials Science and Engineering: A 740-741 (2019) 148-156.

[13] Y. Cao, X. Lin, Q.Z. Wang, S.Q. Shi, L. Ma, N. Kang, W.D. Huang, Microstructure evolution and mechanical properties at high temperature of selective laser melted AlSi10Mg, Journal of Materials Science & Technology 62 (2021) 162-172.

[14] L. Wang, X. Jiang, Y. Zhu, X. Zhu, J. Sun, B. Yan, An approach to predict the residual stress and distortion during the selective laser melting of AlSi10Mg parts, The International Journal of Advanced Manufacturing Technology 97(9) (2018) 3535-3546.

[15] Y. Kok, X.P. Tan, P. Wang, M.L.S. Nai, N.H. Loh, E. Liu, S.B. Tor, Anisotropy and heterogeneity of microstructure and mechanical properties in metal additive manufacturing: A critical review, Materials & Design 139 (2018) 565-586.

[16] L. Girelli, M. Tocci, M. Gelfi, A. Pola, Study of heat treatment parameters for additively manufactured AlSi10Mg in comparison with corresponding cast alloy, Materials Science and Engineering: A 739 (2019) 317-328.

[17] L.F. Wang, J. Sun, X.L. Yu, Y. Shi, X.G. Zhu, L.Y. Cheng, H.H. Liang, B. Yan, L.J. Guo, Enhancement in mechanical properties of selectively laser-melted AlSi10Mg aluminum alloys by T6-like heat treatment, Materials Science and Engineering: A 734 (2018) 299-310.

[18] N.T. Aboulkhair, I. Maskery, C. Tuck, I. Ashcroft, N.M. Everitt, The microstructure and mechanical properties of selectively laser melted AlSi10Mg: The effect of a conventional T6-like heat treatment, Materials Science and Engineering: A 667 (2016) 139-146.

[19] W.H. Kan, Y. Nadot, M. Foley, L. Ridosz, G. Proust, J.M. Cairney, Factors that affect the properties of additively-manufactured AlSi10Mg: Porosity versus microstructure, Additive Manufacturing 29 (2019) 100805.

[20] C. Weingarten, D. Buchbinder, N. Pirch, W. Meiners, K. Wissenbach, R. Poprawe, Formation and reduction of hydrogen porosity during selective laser melting of AlSi10Mg, Journal of Materials Processing Technology 221 (2015) 112-120.

[21] J. Fiocchi, A. Tuissi, P. Bassani, C.A. Biffi, Low temperature annealing dedicated to AlSi10Mg selective laser melting products, Journal of Alloys and Compounds 695 (2017) 3402-3409.

[22] T.-H. Park, M.-S. Baek, H. Hyer, Y. Sohn, K.-A. Lee, Effect of direct aging on the microstructure and tensile properties of AlSi10Mg alloy manufactured by selective laser melting process, Materials Characterization 176 (2021) 111113.

[23] M. Giovagnoli, M. Tocci, A. Fortini, M. Merlin, M. Ferroni, A. Migliori, A. Pola, Effect of different heat-treatment routes on the impact properties of an additively manufactured AlSi10Mg alloy, Materials Science & Engineering A 802 (2021) 140671.

[24] N.E. Uzan, R. Shneck, O. Yeheskel, N. Frage, High-temperature mechanical properties of AlSi10Mg specimens fabricated by additive manufacturing using selective laser melting technologies (AM-SLM), Additive Manufacturing 24 (2018) 257-263.

[25] M. Fousova, D. Dvorsky, M. Vronka, D. Vojtech, P. Lejcek, The use of selective laser melting to increase the performance of AlSi9Cu3Fe alloy, Materials 11(10) (2018).

[26] M. Albu, R. Krisper, J. Lammer, G. Kothleitner, J. Fiocchi, P. Bassani, Microstructure evolution during in-situ heating of AlSi10Mg alloy powders and additive manufactured parts, Additive Manufacturing 36 (2020) 101605.

[27] A.S. Nowick, B.S. Berry, Anelastic Relaxation in Crystalline Solids, Academic Press, New York, 1972.

[28] M.S. Blanter, I.S. Golovin, H. Neuhäuser, H.-R. Sinning, Internal Friction in Metallic Materials, Springer Series in Materials Science, Springer Verlag, Berlin Heidelberg, 2007.

[29] M. Tocci, A. Varone, R. Montanari, A. Pola, Study of high temperature properties of AlSi10Mg ally produced by laser-based powder bed fusion, Materials Science Forum 1016 (2021) 1485-1491.

[30] S. Amadori, E.G. Campari, A.L. Fiorini, R. Montanari, L. Pasquini, L. Savini, E. Bonetti, Automated resonant vibrating reed analyzer apparatus for a non destructive characterization of materials for industrial applications, Mater. Sci. Eng. A 442 (2006) 543-546.

[31] B.D. Cullity, Elements of X-ray diffraction, Second Edition, Addison Wesley Publishing Company INC., Reading, Massachussets, 1977.

[32] B.E. Warren, B.L. Averbach, The effect of cold-work distortion on X-ray patterns, J. Appl. Phys. 21 (1950) 595-599.

[33] G.K. Williamson, R.A. Smallman, Dislocation densities in some annealed and cold-worked metals from measurements on the X-ray debye-scherrer spectrum, Phil. Mag. 1 (1956) 34-46.

[34] T.S. Kê, Experimental evidence of the viscous behaviour of grain boundaries in metals, Phys. Rev. 71 (1947) 533-546

[35] JCPDS-International Centre for Diffraction Data, Newtown Square, PA 19073, USA.

[36] A. Pichler, E. Arzt, Internal friction in F.C.C. alloys due to solute drag on dislocations- I. A model for the effect of core diffusion, Acta Metall. et Mater., Vol. 42, No. 1 1, (1994) 3785-3800.

[37] A. Pichler, M. Weller, E. Arzt, Internal friction in F.C.C. alloys due to solute drag on dislocation-II. Experimental studies on AI-Si alloys, Acta Metall. et Mater. Vol. 42, No. 11, (1994) 3801-3809.

[38] M. Atodiresei, G. Gremaud, R. Schaller, Study of solute atom-dislocation interactions in Al-Mg alloys by mechanical spectroscopy, Materials Science and Engineering A 442 (2006) 160-164.

[39] M. Benyahi, M. Gerland, C. Belamri, A. Rivière, Low Frequency Relaxation Effect Observed in Al-Mg Alloy, Solid State Phenom. 184, 149–154 (2012).

[40] I.S. Golovin, A.S. Bychkov, S.V. Medvedeva, X.S. Hu, M.Y. Zheng, Mechanical Spectroscopy of Al-Mg Alloys, The Physics of Metals and Metallography, 2013, Vol. 114, No. 4, 327-338.

[41] I.S. Golovin. S. Jäger, V.A. Semin, G.V. Serzhantova, H.-R. Sinning, O.A. Sokolova, F. Stein, S.A. Golovin., Snoek-type and Zener relaxation in Fe-Si-Al Alloys, Solid State Phenomena 137 (2008) 69-82.

[42] I.S. Golovin, A.V. Mikhaylovskaya, H.-R. Sinning, Role of the β-phase in grain boundary and dislocation anelasticity in binary Al–Mg alloys, J. Alloys Compd. 577 (2013) 622–632.

[43] A.V. Mikhaylovskaya, V.K. Portnoy, A.G. Mochugovskiy, M.Yu. Zadorozhnyy, N.Yu. Tabachkova, I.S. Golovin, Effect of homogenisation treatment on precipitation, recrystallisation and properties of Al-3% Mg-TM alloys (TM = Mn, Cr, Zr), Materials and Design 109 (2016) 197-208.
[44] C. Amrane, D. Hamana, I.S. Golovin, Internal friction sensitivity to precipitation in Al-12 wt% Mg alloy, Materials Characterization 134, (2017) 49-54.
[45] W.B. Pearson, A Handbook of Lattice Spacings and Structures of Metals and Alloys, Pergamon Press, 1967.
[46] S. Marola, D. Manfredi, G. Fiore, M.G. Poletti, M. Lombardi, P. Fino, L. Battezzati, A comparison of Selective Laser Melting with bulk rapid solidification of AlSi10Mg alloy, J. Alloys Compd. 742 (2018) 271–279.
[47] T. S. Kê, Q. Tan, Internal friction peak associated with the enhanced re-orientation of split interstitials of magnesium atoms in close vicinity of the dislocation kinks in aluminium, Acta Metall. et Mater., Vol. 39, No. 5, (1991) 885-891.
[48] L.J. Gibson, M.F. Ashby, *Cellular solids. Structure and properties*, 2nd Edition., Cambridge University Press: Cambridge, 1989.

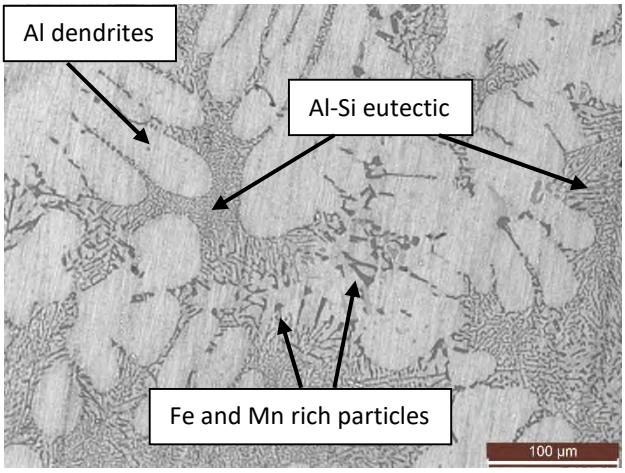

a)

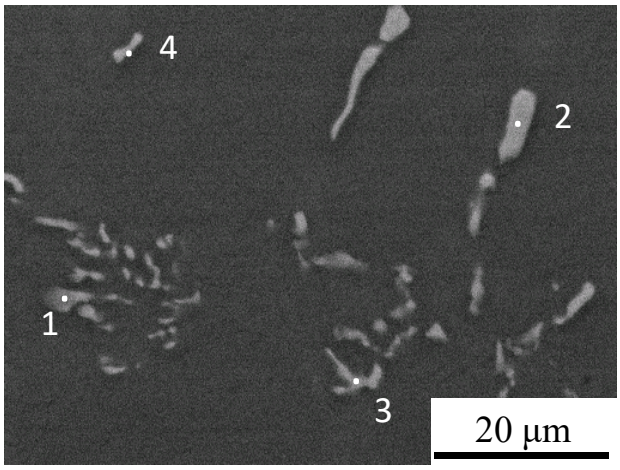

b)

Wt. %	Al	Si	Mn	Fe
1	79.44	7.15	5.87	7.54
2	65.08	9.05	9.35	16.52
3	72.37	11.41	7.67	8.55
4	70.70	10.42	7.65	11.23

c)

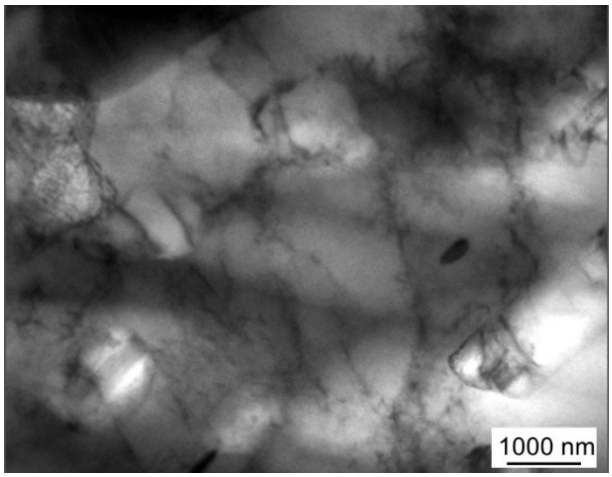

d)

Figure 1. As-cast (AC) alloy: LM micrograph in (a) shows the Al dendritic structure surrounded by a fine Al-Si eutectic and particles with elongated shape. The morphology of these particles is displayed at higher magnification in the SEM image in (b). Some of them, indicated in (b), have been analyzed by EDS and the compositions are reported in (c). TEM micrograph in (d) displays the cell structure formed by dislocations in the Al matrix.

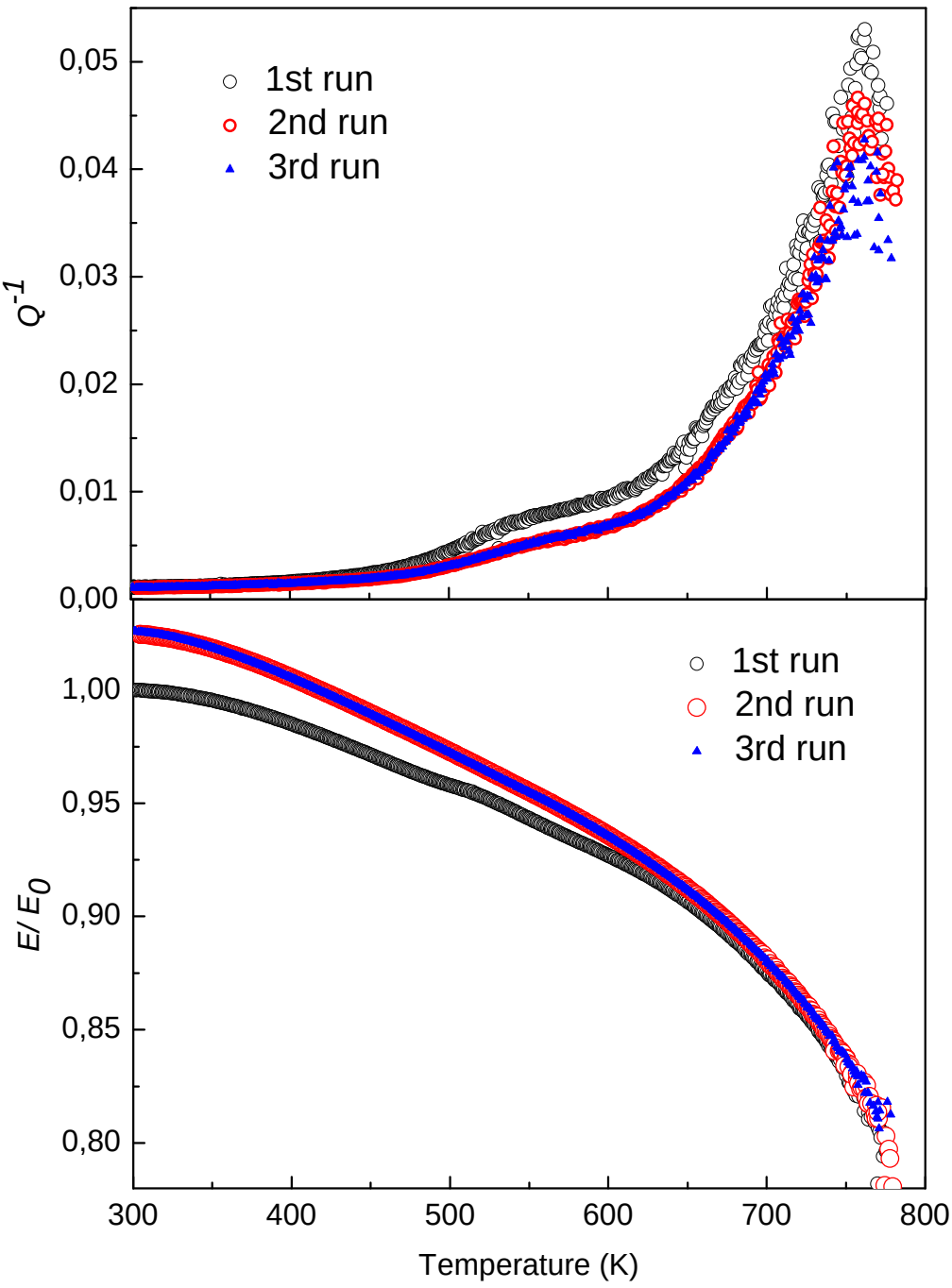

Figure 2. As-cast (AC) alloy: Q^{-1} and dynamic modulus E vs. temperature measured in three successive test runs. Dynamic modulus values are normalized to the initial value E_0 (at room temperature, before the 1st run). The initial resonance frequency at room temperature is 670 Hz.

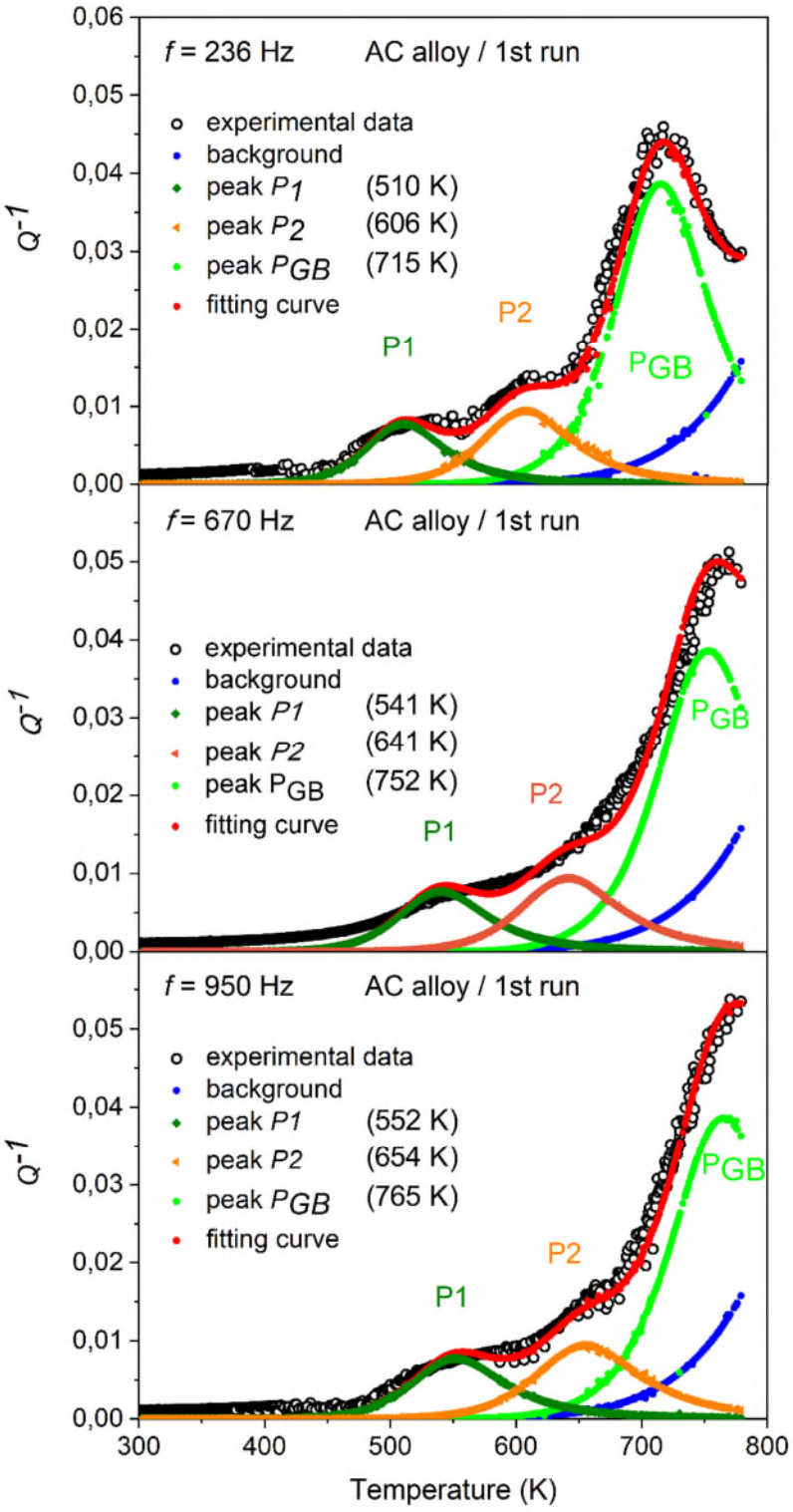

Figure 3. As-cast (AC) alloy: the Q^{-1} curves vs. temperature (open circles) recorded with different resonance frequencies (236, 670 and 950 Hz) have been fitted by the sum of four contributions, namely the background (blue points), the peaks *P1* (olive points), *P2* (orange points) and P_{GB} (green points). The fitting curve is indicated by red points. The central positions of *P1*, *P2* and P_{GB} peaks, reported in each graph, change with the frequency.

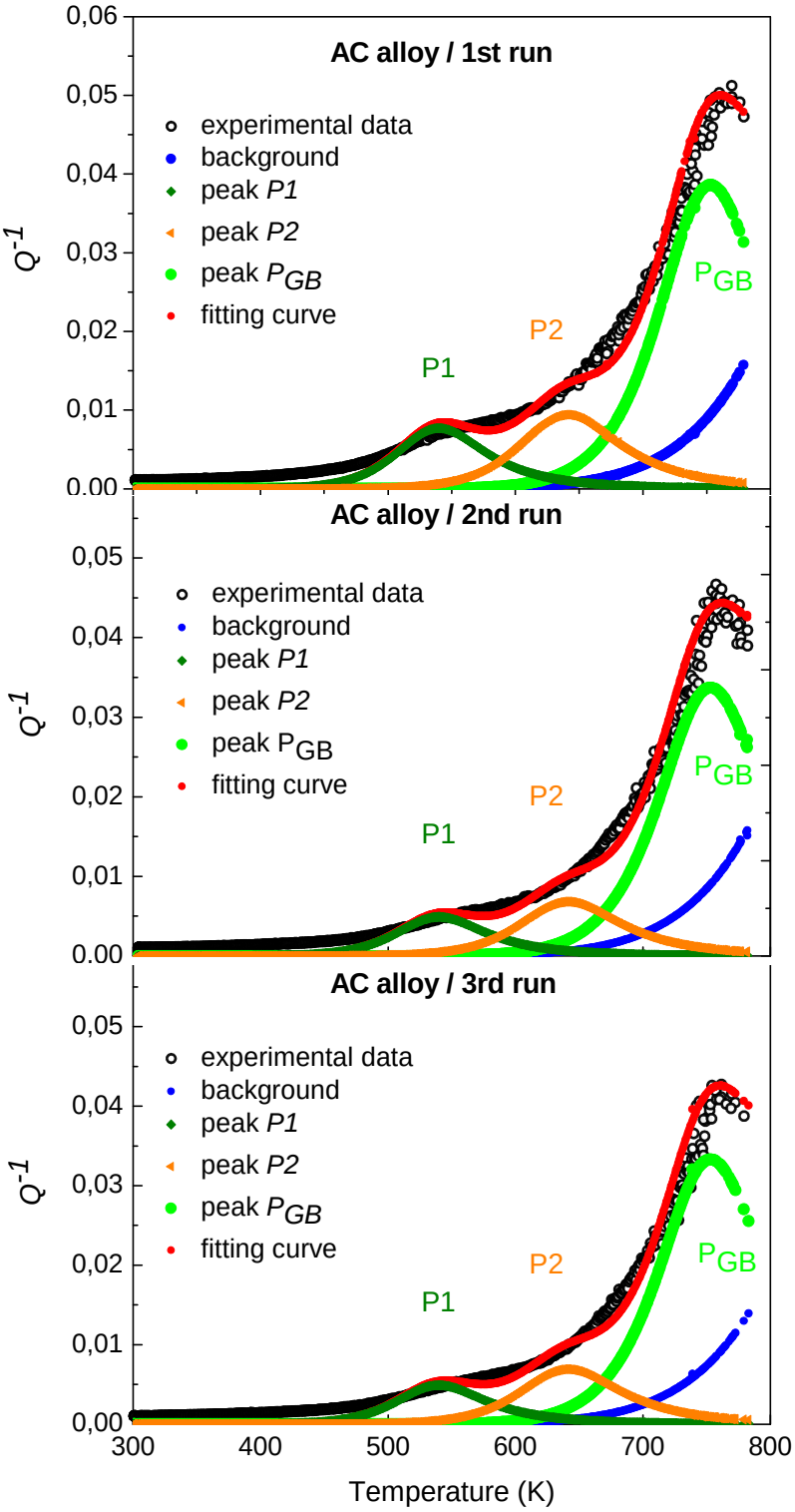

Figure 4. As-cast (AC) alloy: the Q^{-1} curves vs. temperature recorded in 1st, 2nd and 3rd runs (open circles) have been fitted by the sum of four contributions, namely the background (blue points), the peaks *P1* (olive points), *P2* (orange points) and P_{GB} (green points). The fitting curve is indicated by red points. The resonance frequency is 670 Hz.

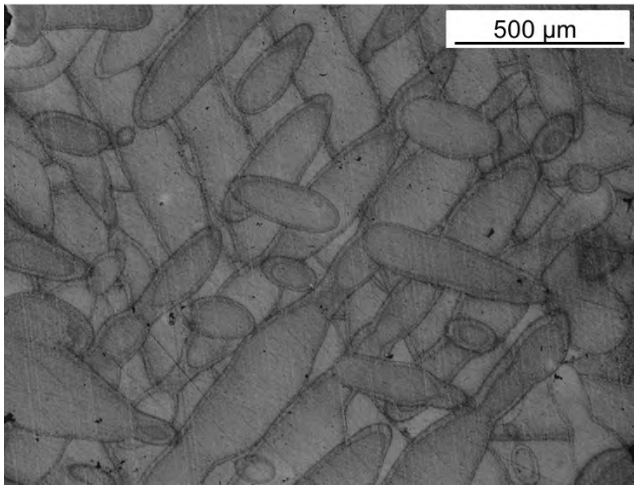

(a)

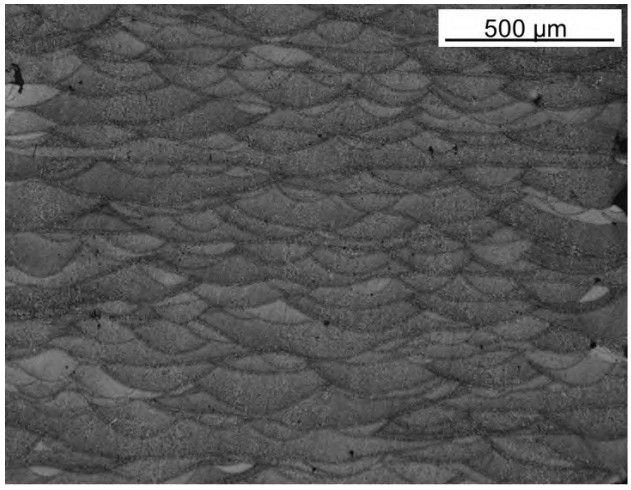

(b)

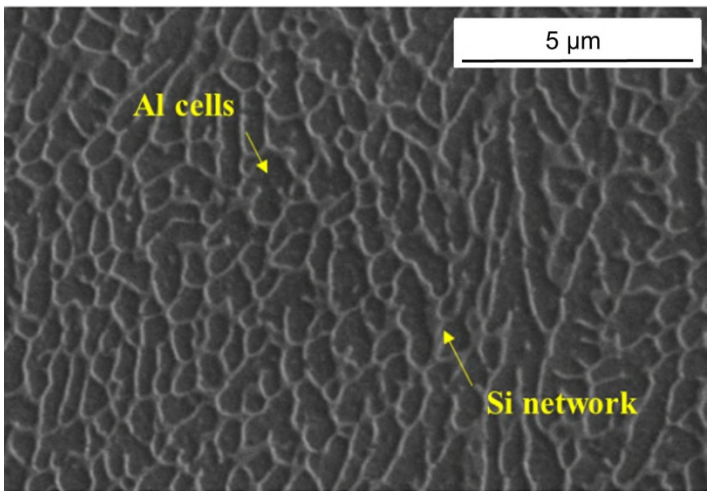

(c)

Figure 5. Additive manufactured (AM) alloy: horizontal and vertical sections are shown in (a) and (b-c), respectively.

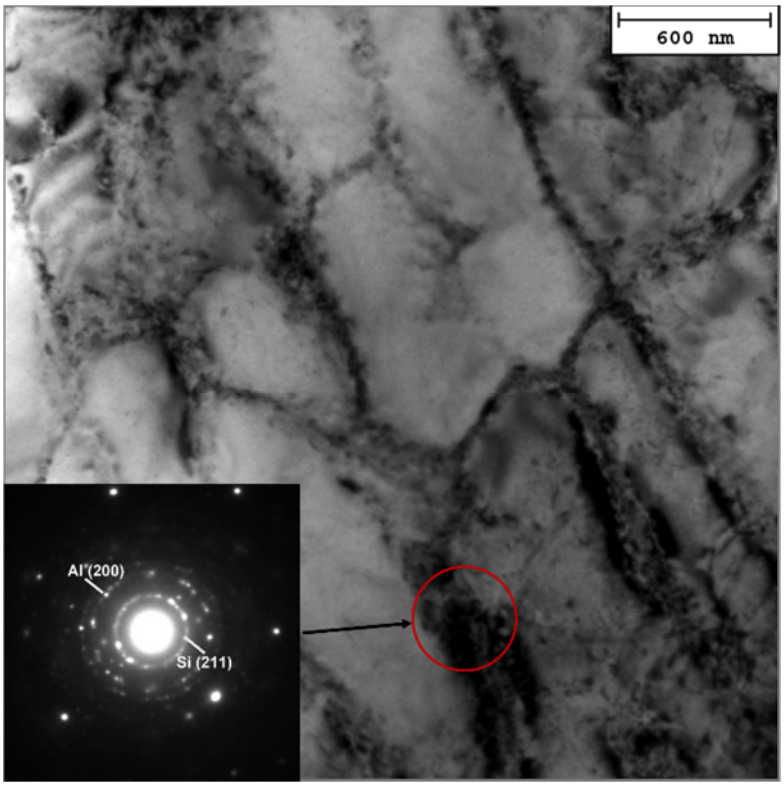

(a)

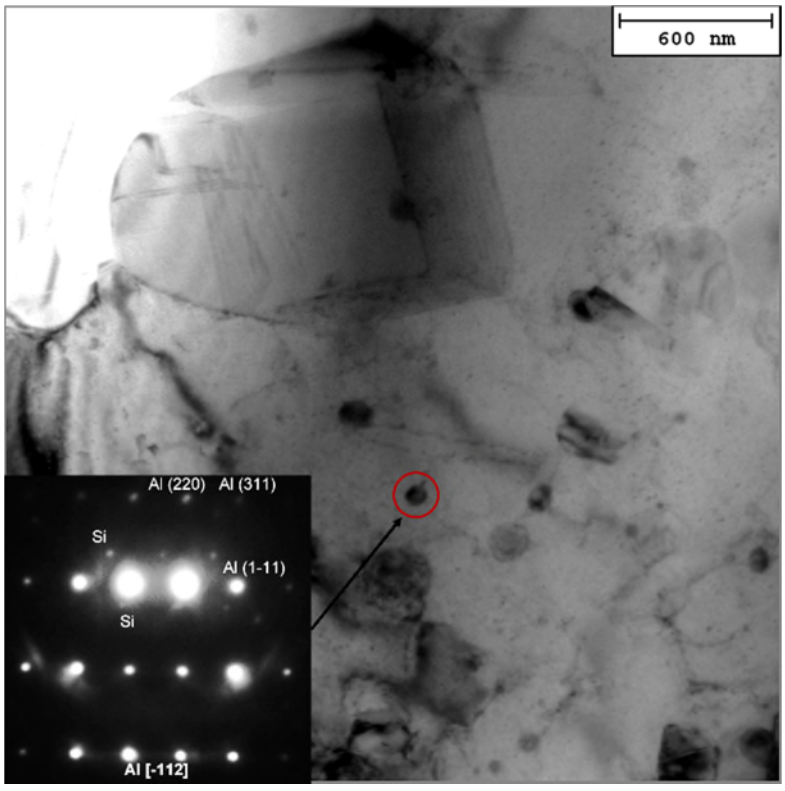

(b)

Figure 6. Additive manufactured (AM) alloy: TEM micrograph in (a) shows elongated cells of ~ 400 nm while rounded and irregular shaped precipitates of very small size (100-150 nm). Insets in (a) and (b) shows SAEDPs taken from the rounded red area of the micrographs. Both SAEDPs reveal the presence of Si particles. In (b) the Al-matrix zone axis is Al [-112].

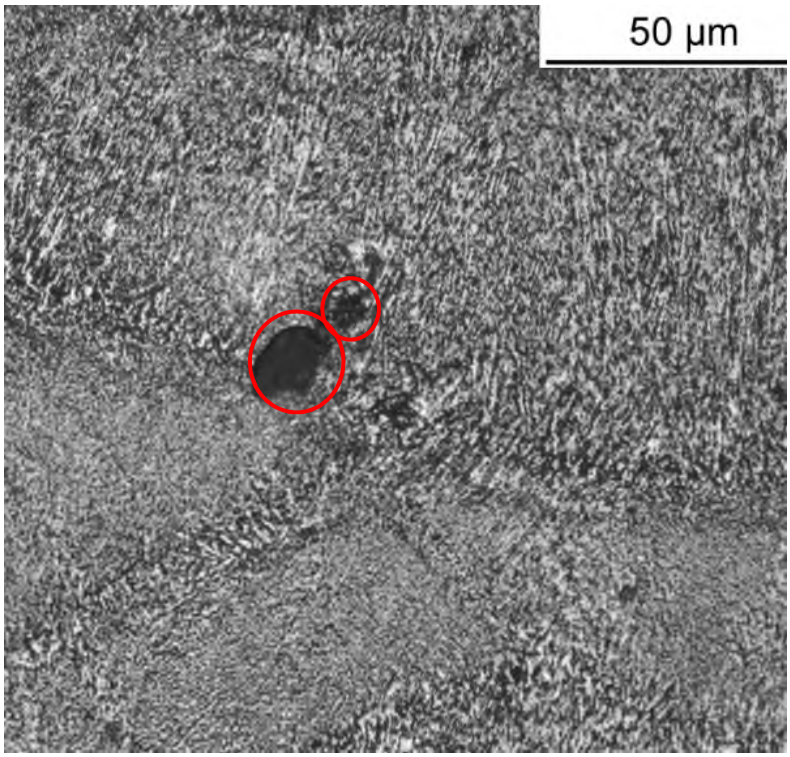

(a)

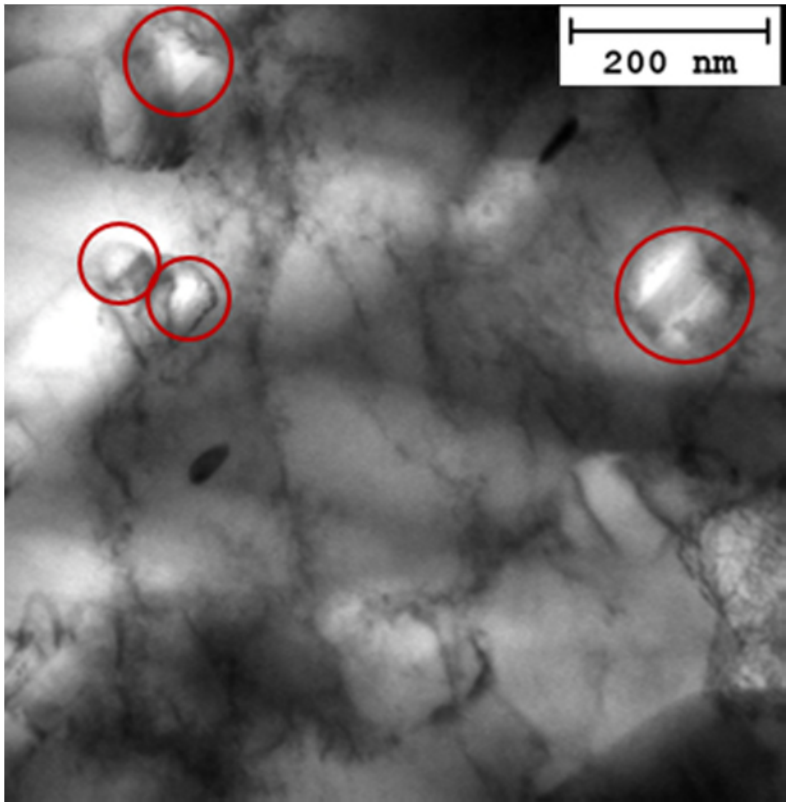

(b)

Figure 7. Additive manufactured (AM) alloy: pores of great (SEM micrograph in a) and small size (TEM micrograph in b) are evidenced by red circles.

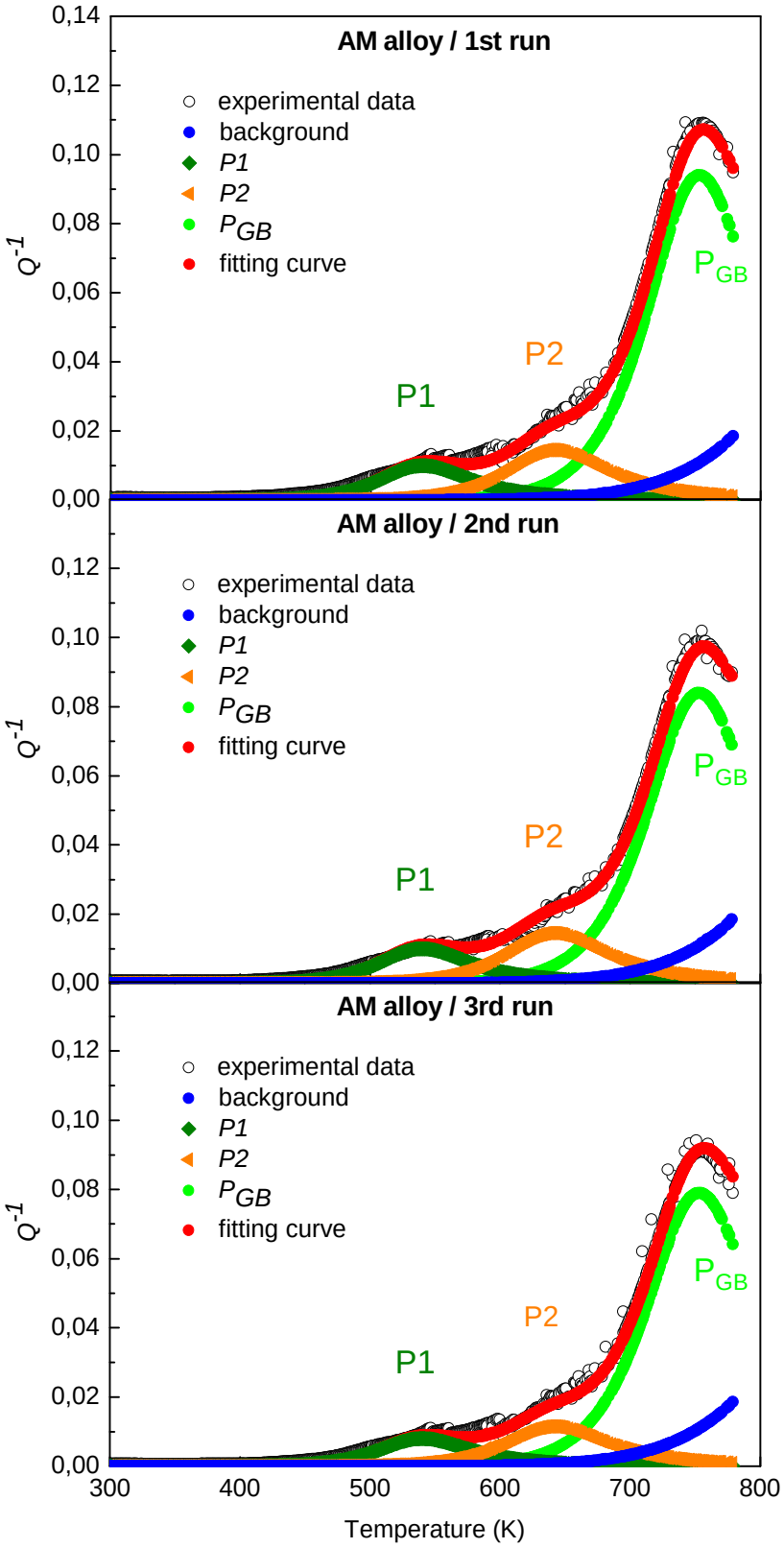

Figure 8. Additive manufactured (AM) alloy: the Q^{-1} curves vs. temperature recorded in 1st, 2nd and 3rd runs (open circles) have been fitted by the sum of four contributions, namely the background (blue points), the peaks *P1* (olive points), *P2* (orange points) and P_{GB} (green points). The fitting curve is indicated by red points. The resonance frequency is 670 Hz.

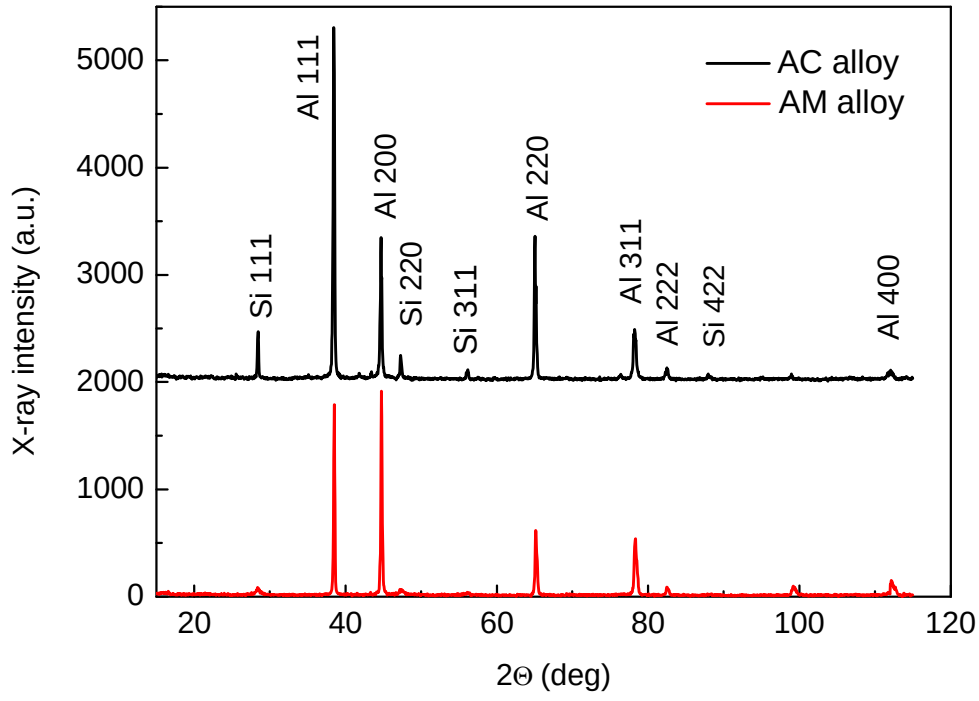

(a)

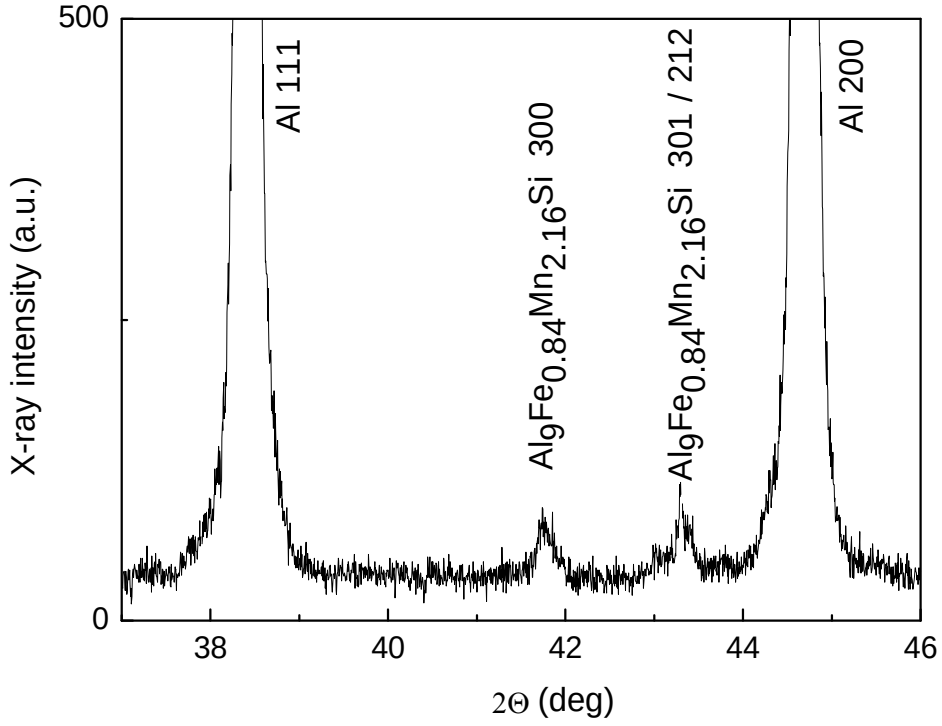

(b)

Figure 9. XRD patterns of as-cast (AC) and additive manufactured (AM) alloys (a) recorded with 2θ steps of 0.05° and counting time per step of 2 s. Figure (b) displays a part of the XRD pattern of as-cast (AC) alloy recorded with higher resolution (2θ steps of 0.005°) and longer counting time (20 s) to evidence two weak peaks which result to correspond to the $Al_9Fe_{0.84}Mn_{2.16}Si$ compound.

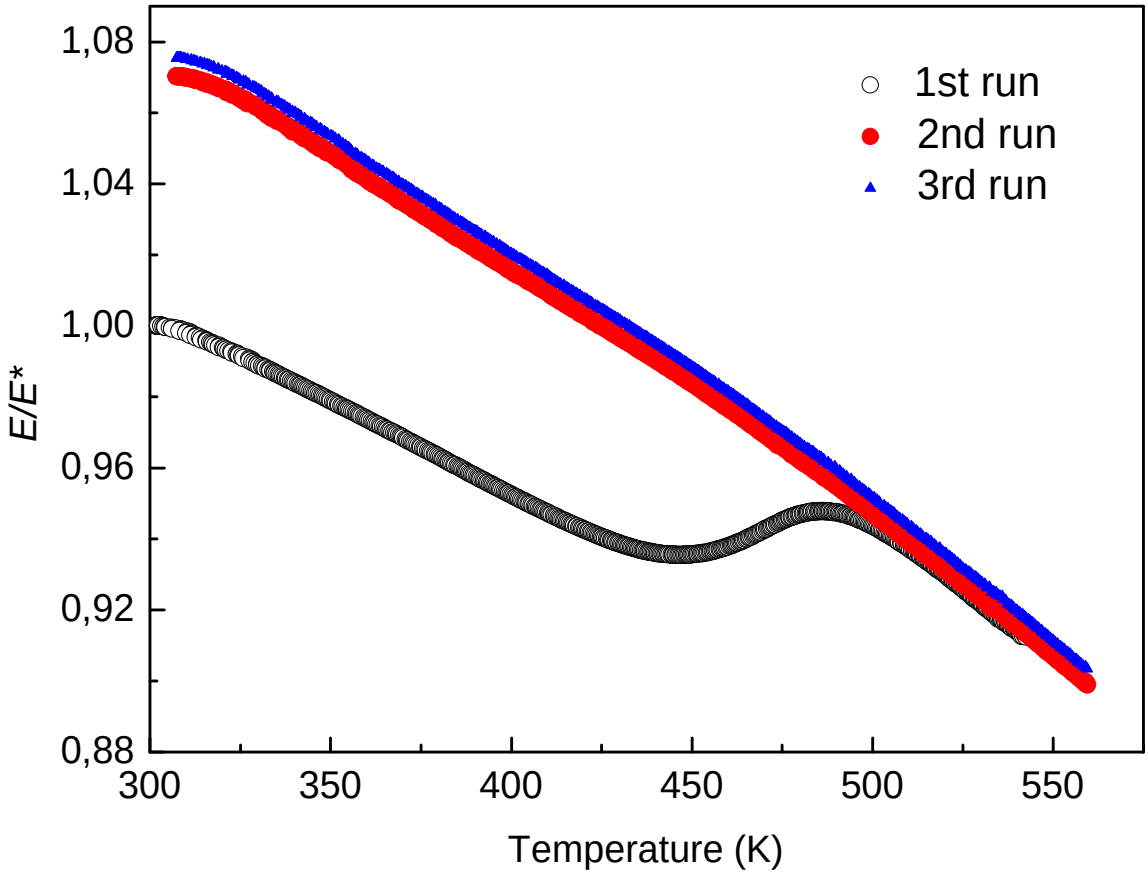

Figure 10. Dynamic modulus *E* vs. temperature of an additive manufactured (AM) sample measured in three successive test runs. The values of dynamic modulus are normalized to the value *E** measured at room temperature in the 1st test run.

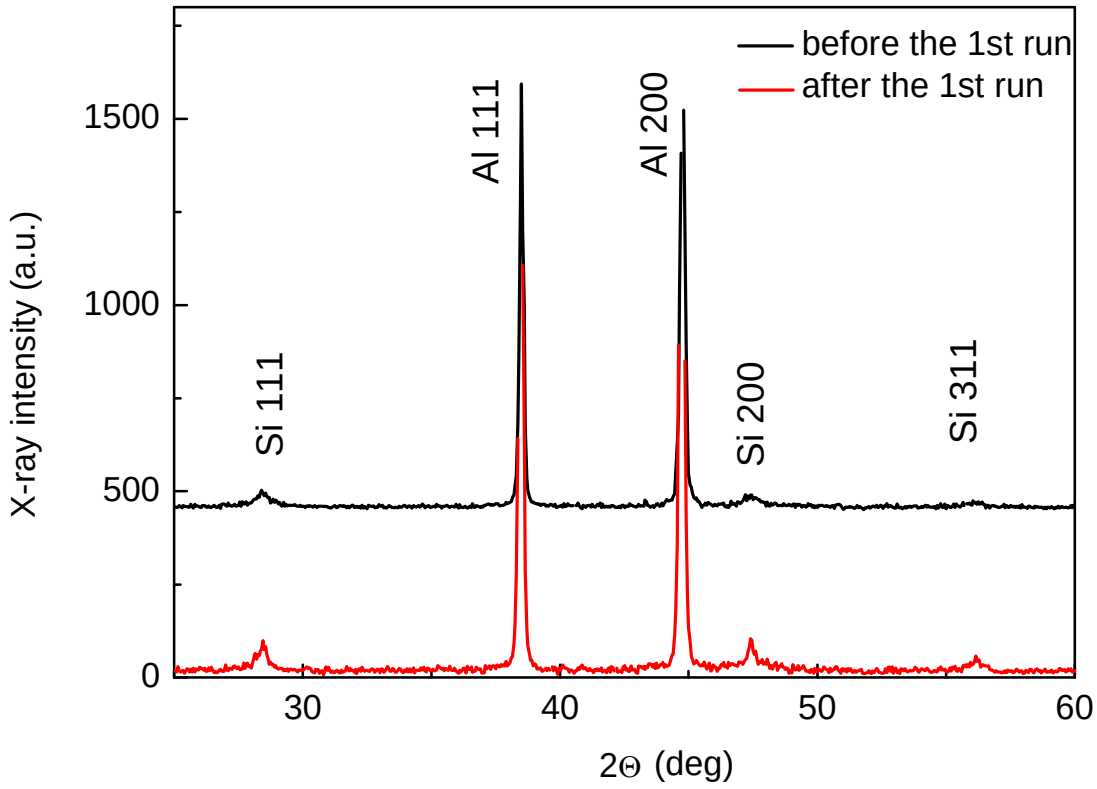

Figure 11. XRD patterns of the additive manufactured (AM) alloy before and after the 1st test run.

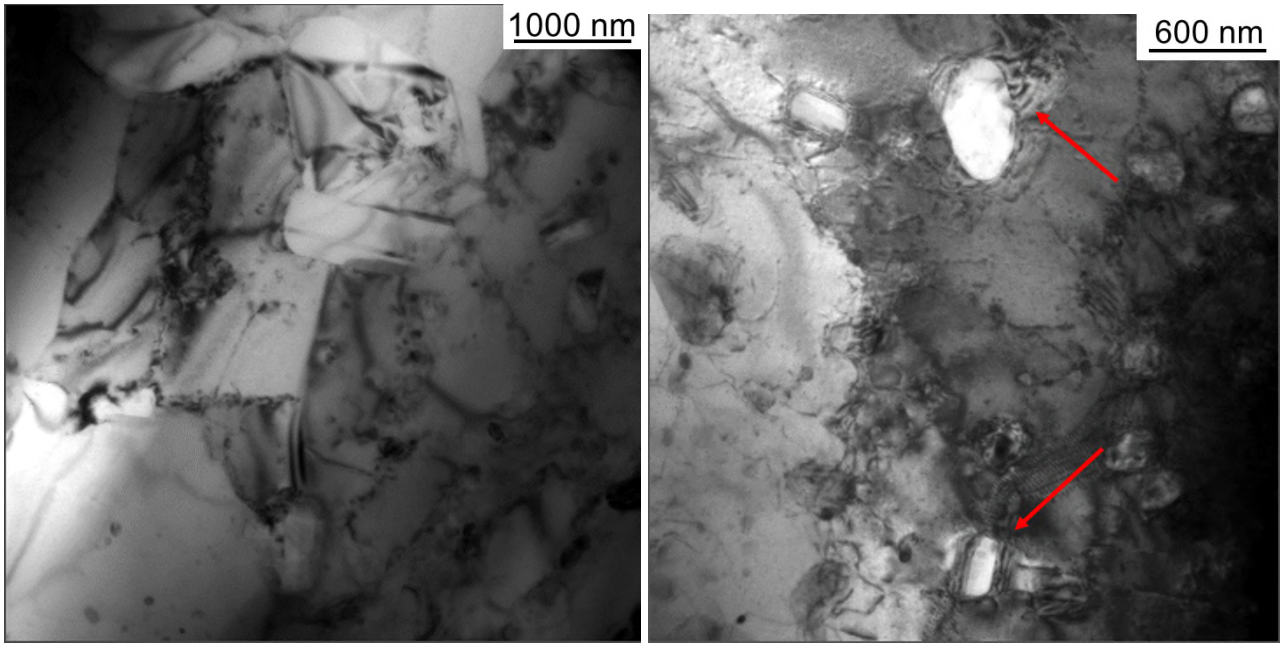

(a) (b)

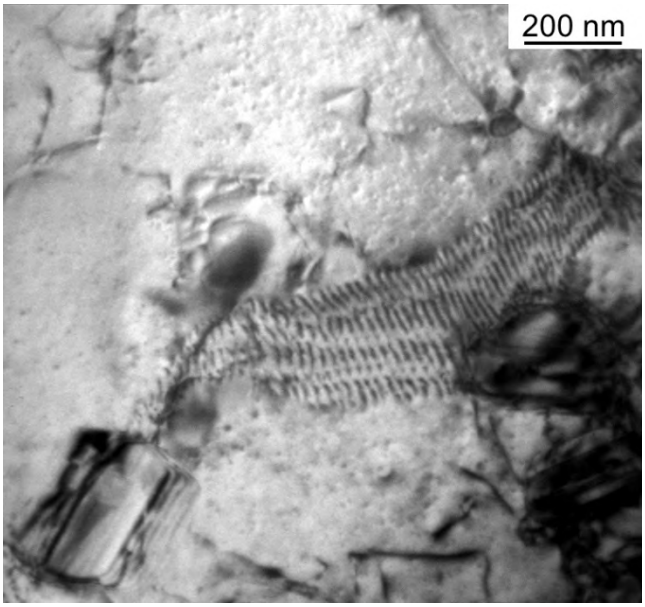

(c)

Figure 12. TEM images of additive manufactured (AM) alloy after the 1st test run. Elongated cells have been replaced by equiaxed cells of larger size (a). Pores of large size are indicated by red arrows (b). In (c) an array of kinked dislocations is observed.

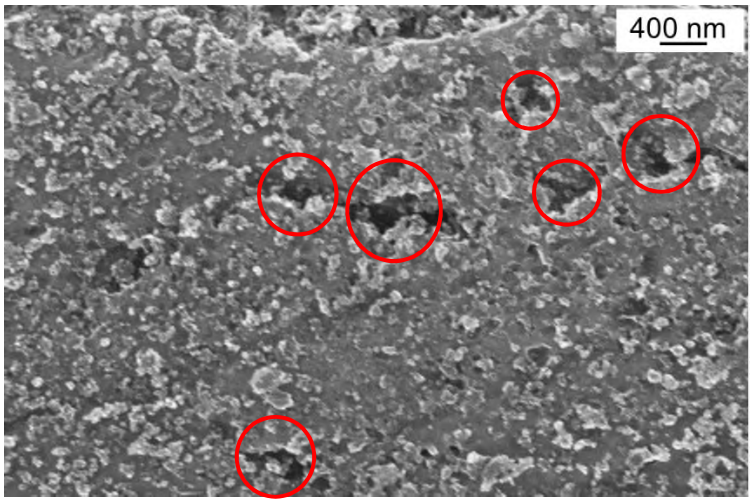

(a)

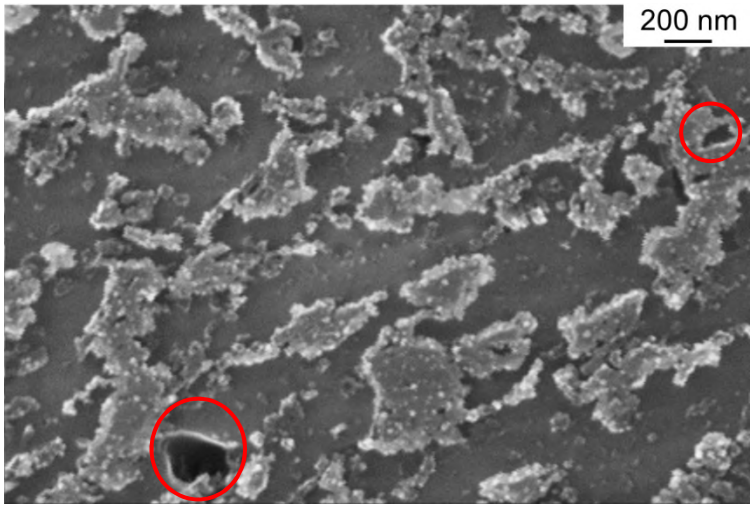

(b)

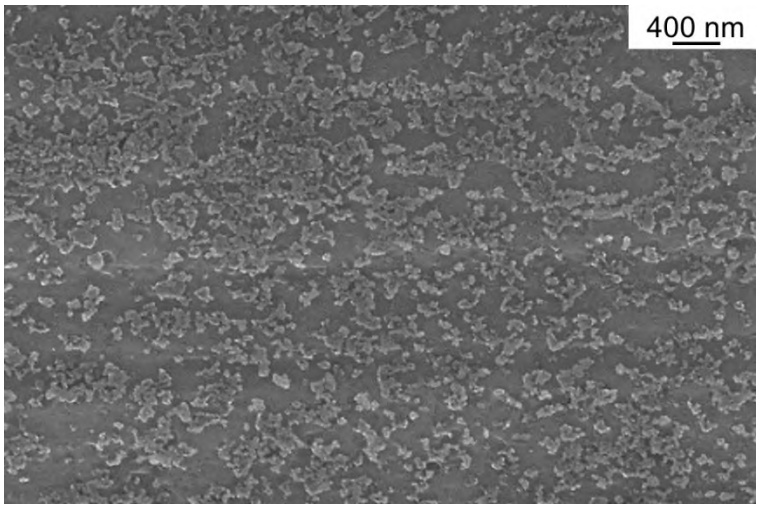

(c)

Figure 13. FEG-SEM micrographs of as-built additive manufactured (AM) alloy at increasing magnification (a and b) and after an MS test run with heating up to 485 K (c). Pores are indicated by red circles in (a) and (b).